JOM Journal of Optical Microsystems

RESEARCH PAPER

Hybrid all-dielectric phase-change metasurfaces for tunable waveplate

Xingling Pan,[a] Ziru Cai,[a] Zhiming Chen,[a,*] Yingtao Ding,[a] Ziwei Zheng,[b] and Fei Ding[c,*]

[a]Beijing Institute of Technology, School of Integrated Circuits and Electronics, Beijing, China
[b]Zhejiang Wanli University, Digital Industry Research Institute, Ningbo, China
[c]University of Southern Denmark, Centre for Nano Optics, Odense, Denmark

ABSTRACT. Metasurfaces have attracted immense interest across various scientific disciplines due to their ability to manipulate light wave parameters with numerous functionalities. However, these functionalities have historically been static, lacking the capability for dynamic, real-time control. In this study, we introduce a highly efficient, tunable waveplate by incorporating a thin layer of the phase change material Sb_2Se_3 into a silicon all-dielectric metasurface. This structure demonstrates the ability to transition from a half-waveplate to a quarter-waveplate as Sb_2Se_3 shifts from an amorphous to a crystalline state at the telecom wavelength of 1.55 μm. Remarkably, it maintains consistent performance across a range of rotation angles. In addition, we have performed comprehensive electro-thermal simulations to validate the phase change process, confirming the practical feasibility of this technology. This tunable metasurface represents a significant advancement in adaptive photonics, offering customizable and sophisticated functionalities.

 [DOI: 10.1117/1.JOM.4.3.031206]

Keywords: all-dielectric metasurface; Sb_2Se_3; tunable waveplate; electro-thermal simulation

Paper 24002SS received Jan. 30, 2024; revised May 14, 2024; accepted May 21, 2024; published Jun. 8, 2024.

1 Introduction

Metasurfaces, subwavelength nanostructures arranged on a two-dimensional plane, have garnered increasing attention due to their ultrathin profiles and exceptional ability to manipulate scattered light fields.[1–3] Historically, these metasurfaces have demonstrated remarkable capabilities, including polarization conversion,[4,5] beam steering,[6,7] vortex-beam generation,[8,9] and more.[10–12] All-dielectric metasurfaces,[13–15] composed of high refractive index materials such as silicon (Si) for meta-atoms, exhibit multiple Mie responses driven by displacement currents, rendering them immune to ohmic losses.[16–18] However, most all-dielectric metasurfaces are passive, exhibiting static responses dictated by material compositions and configuration, which prevents them from fulfilling the demand for real-time tunability.

To address the evolving needs of adaptive photonic integrated systems, research has pivoted toward active all-dielectric metasurfaces equipped with dynamic control capabilities. Efforts include integrating Si nanodisk metasurface with liquid crystals,[19–21] although the considerable thickness of liquid crystal solutions (i.e., the order of micrometers) often results in a significantly bulkier device. Another approach involves dynamically tuning the all-dielectric metasurface through temperature-dependent changes in the refractive index of Si,[22,23] but this method suffers

*Address all correspondence to Zhiming Chen, czm@bit.edu.cn; Fei Ding, feid@mci.sdu.dk

from a relatively slow tuning speed. Therefore, there is an imperative need for tunable all-dielectric metasurfaces that combine high efficiency, rapid tuning, and compactness.

In this work, we introduce a tunable metasurface-based waveplate (meta-WP) operating in the near-infrared region by incorporating a thin layer of phase change material Sb_2Se_3 within a Si nano-cube. This design allows the meta-WP to alternate functions between a half-waveplate (HWP) and a quarter-waveplate (QWP) at a telecom wavelength of 1.55 μm while maintaining consistent performance across various rotation angles. Unlike the commonly used phase change material germanium antimony telluride compounds,[24–27] Sb_2Se_3 offers lower losses at both amorphous and crystalline states in the near-infrared band.[28–30] Notably, Sb_2Se_3 has nearly zero loss in both amorphous and crystalline states and undergoes a significant refractive index change ($\Delta n \sim 1$) between these two states at the telecommunication C-band (1.55 μm).[31] These characteristics ensure superior performance for our designed meta-waveplate. In addition, we present a detailed Joule heating analysis to confirm the reversible tunability of the meta-WP, where a graphene microheater precisely controls the Sb_2Se_3 phase transition. Our proposed hybrid nanostructure presents a significant advancement for integrated adaptive photonics, promising high efficiency and versatile switchable functionalities.

2 Results and Discussion

The operating principle of the proposed tunable waveplates is illustrated in Fig. 1, where periodic $Si - Sb_2Se_3 - Si$ sandwich meta-atoms stand on top of a quartz substrate. At the amorphous state, a circularly polarized (CP) incident beam transforms into its cross-polarized counterpart with reversed handedness after transmitting through the $Si - Sb_2Se_3 - Si$ metasurface, acting as an HWP. Upon triggering Sb_2Se_3 into its crystalline state, the metasurface functions as a QWP that converts CP incident beams into the ± 45 deg oriented linearly polarized (LP) beams.

From a microscopic perspective, the corresponding optical transmission characteristics of the $Si - Sb_2Se_3 - Si$ meta-atom can be described through the Jones matrix

$$T = \begin{pmatrix} t_{xx} & 0 \\ 0 & t_{yy} \end{pmatrix}, \tag{1}$$

where $t_{xx} = |t_{xx}|e^{i\delta_{xx}}$ and $t_{yy} = |t_{yy}|e^{i\delta_{yy}}$ are the transmission coefficients under x- and y-polarized excitations, which are mainly determined by the lateral dimensions along x- and y-directions, respectively. Specifically, $|t_{xx}|$ and $|t_{yy}|$ represent transmission amplitudes, whereas δ_{xx} and δ_{yy} stand for the phase delays. If the transmission amplitudes are equal (e.g., $|t_{xx}| = |t_{yy}|$) and the relative phase difference $\Delta\delta = \delta_{yy} - \delta_{xx}$ equals ± 90 or 180 deg, a QWP or an HWP could be obtained accordingly.

To determine the anticipated meta-atom dimensions, three-dimensional (3D) full-wave simulations were carried out using the commercially available software COMSOL Multiphysics (version 6.0). Throughout simulations, periodic boundary conditions are implemented for the $Si - Sb_2Se_3 - Si$ unit cell in both x- and y-directions. Perfectly matching layers are introduced

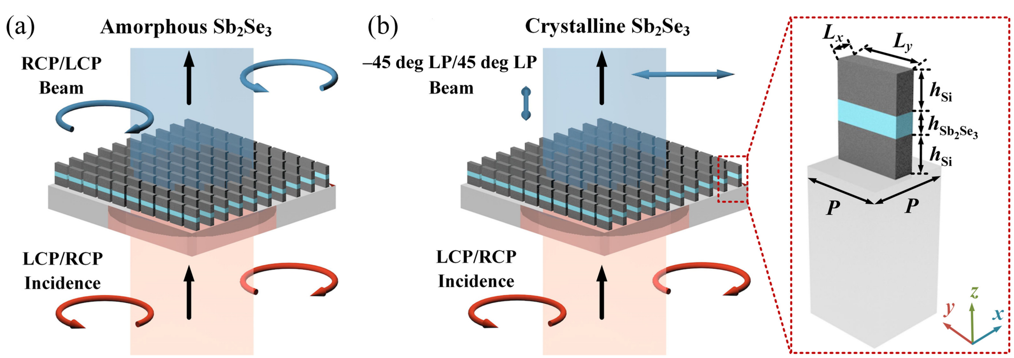

Fig. 1 Working principle of the proposed tunable meta-WP. (a) The designed metasurface works as an HWP when Sb_2Se_3 is in the amorphous phase. (b) The designed metasurface works as a QWP when Sb_2Se_3 is in the crystalline phase. The inset shows the aerial view of the designed unit cell on the quartz substrate.

above and below the unit cell to truncate the simulation domain. The quartz substrate is assumed as a lossless dielectric material with a constant refractive index of 1.44, whereas the refractive index of amorphous Si is considered 3.6147 + 0.064753i. Moreover, the measured refractive indices of Sb_2Se_3 in the amorphous and crystalline states are 3.306 and 4.3281 + 0.000021i, respectively, at the target wavelength of 1.55 μm.[30] The periodicity P of the $Si - Sb_2Se_3 - Si$ meta-atom is set as 660 nm to eliminate any unwanted diffraction order. The height h of the Si and Sb_2Se_3 brick is set as 289 and 155 nm, respectively, ensuring sufficient phase response and acceptable transmittance under two different states of Sb_2Se_3. Figure 2 presents the simulated transmission amplitudes and phase distributions of the $Si - Sb_2Se_3 - Si$ meta-atom under x-polarized excitation for the two states. The side dimensions (i.e., l_x and l_y) vary from 100 to 600 nm at a 5 nm interval, whereas other geometrical parameters remain constant. The optimized dimensions of the $Si - Sb_2Se_3 - Si$ meta-atom are determined to be $l_x = 165$ nm, $l_y = 550$ nm, marked in Fig. 2.

Figure 3 shows the transmission amplitudes ($|t_{xx}|$ and $|t_{yy}|$) and phase differences ($\Delta\delta$) under x- and y-polarized incidences as a function of wavelength for both amorphous and crystalline Sb_2Se_3. In the amorphous state, $|t_{xx}|$ and $|t_{yy}|$ are found to be 0.975 and 0.933, respectively, with a phase difference $\Delta\delta$ of -179.47 deg at the operation wavelength of 1.55 μm. This is consistent with the requirement of conventional HWPs with equal transmission amplitudes and 180 deg phase retardation between two orthogonal LP beams. Upon Sb_2Se_3 transitioning into the crystalline state, a phase difference $\Delta\delta$ of 86 deg is induced with the corresponding $|t_{xx}|$ of 0.972 and $|t_{yy}|$ of 0.918. Moreover, $|t_{xx}|$ and $|t_{yy}|$ maintain high values of above 0.9 within the wavelength range of 1.53 and 1.57 μm despite the states of Sb_2Se_3, whereas the relative phase differences $\Delta\delta$ are found to be 180 deg ± 10 deg and 90 deg ± 10 deg for the amorphous and crystalline states, respectively, demonstrating the functional switching from an HWP to a QWP for the designed $Si - Sb_2Se_3 - Si$ metasurface with an operating bandwidth of ~40 nm centered at 1.55 μm.

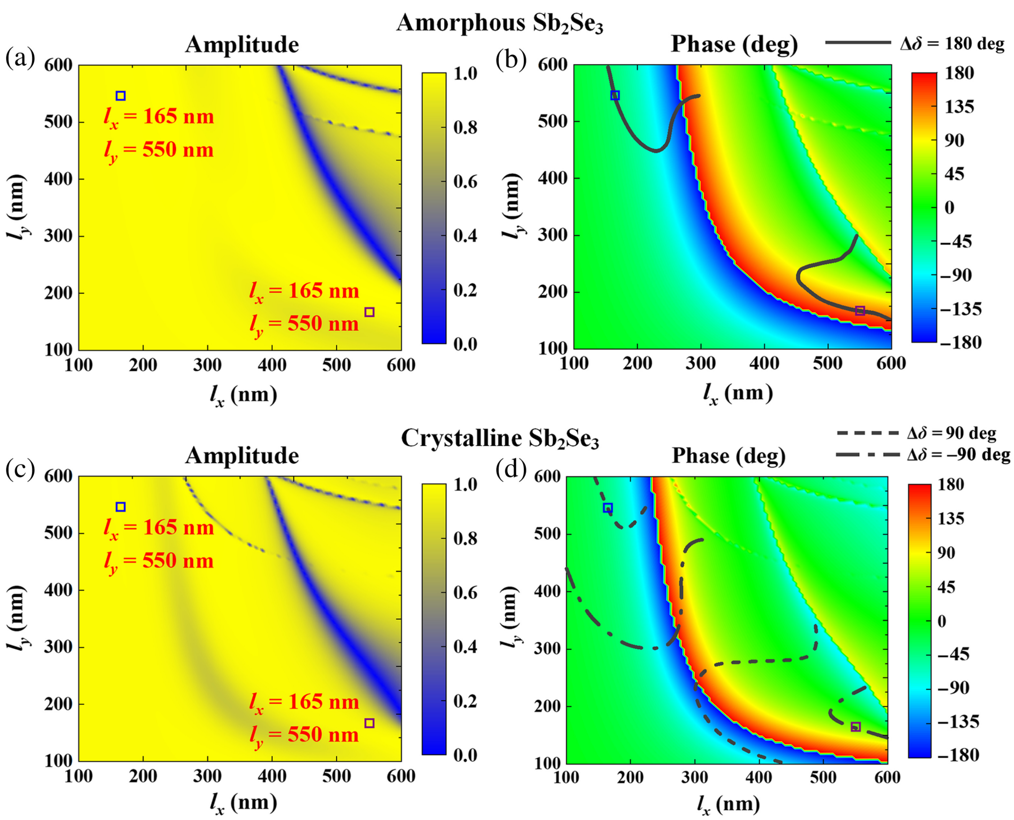

Fig. 2 (a) Simulated and (c) transmission amplitudes and (b) and (d) phase distributions of the $Si - Sb_2Se_3 - Si$ meta-atom as a function of the lateral dimensions for the incident x-polarized wave at $\lambda = 1.55$ μm when Sb_2Se_3 is at the (a), (b) amorphous and (c), (d) crystalline states. The complex transmission coefficient for the y-polarized incident can be obtained by mirroring the map along the line of $l_x = l_y$.

The degree of linear polarization (DoLP), degree of circular polarization (DoCP), and angle of linear polarization (AoLP) are vital physical parameters of the detected light, inferred from Stokes parameters $\begin{pmatrix} S_0 \\ S_1 \\ S_2 \\ S_3 \end{pmatrix}$:[32]

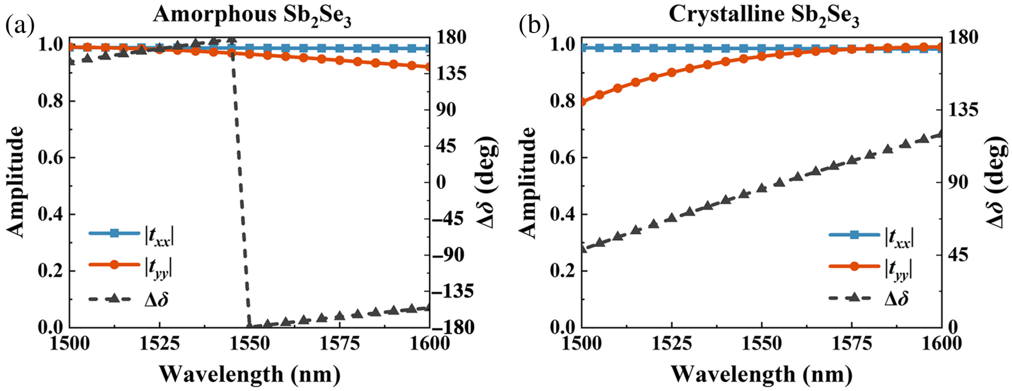

Fig. 3 Simulated transmission amplitudes ($|t_{xx}|$ and $|t_{yy}|$) and the relative phase differences ($\Delta\delta$) under x- and y-polarized excitations at the (a) amorphous and (b) crystalline states.

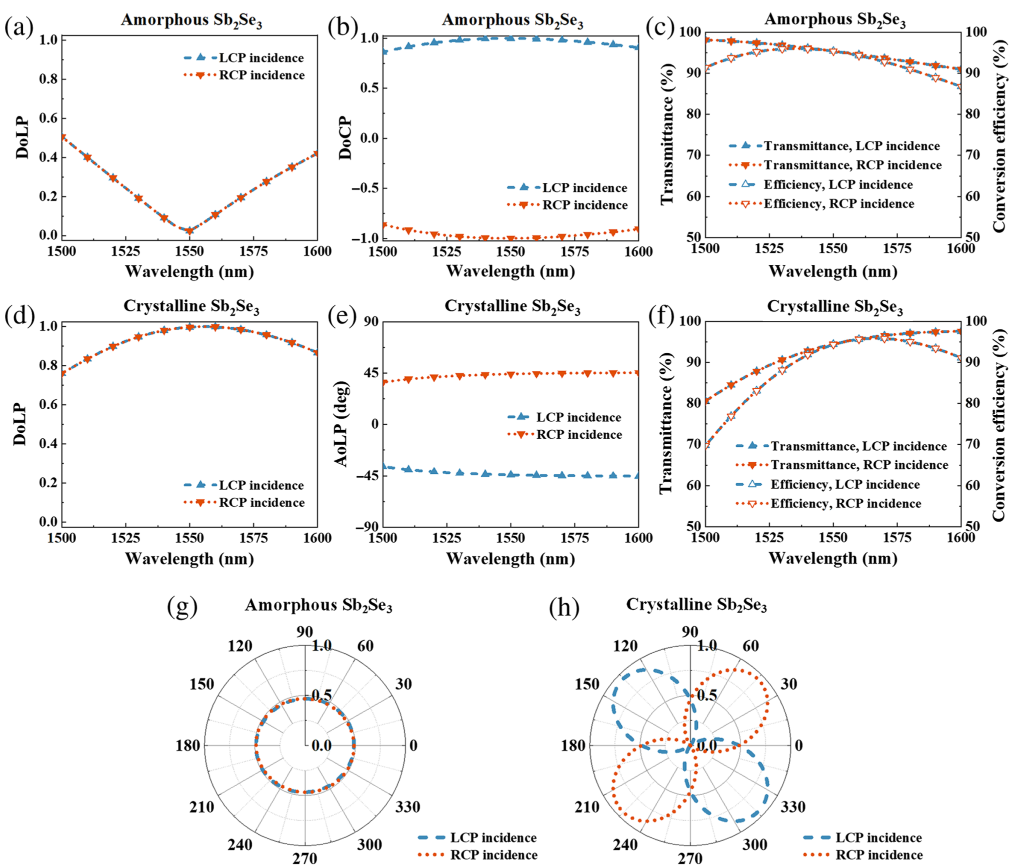

Fig. 4 Performance of the tunable meta-WP. (a) DoLPs and (b) DoCPs of the transmitted beams under CP excitations at the amorphous state. (d) DoLPs and (e) AoLPs of the transmitted beams under CP excitations at the crystalline state. (c), (f) The transmittance and conversion efficiency of the transmitted beams in (c) HWP and (f) QWP mode. (g), (h) Polarization state diagrams of the transmitted beams at the (g) amorphous and (h) crystalline states at the design wavelength of 1.55 μm.

$$\text{DoLP} = \sqrt{(S_1^2 + S_2^2)}/S_0, \tag{2}$$

$$\text{DoCP} = S_3/S_0, \tag{3}$$

$$\text{AoLP} = \tan^{-1}(S_2/S_1)/2. \tag{4}$$

To further validate the polarization conversion performance of the designed $Si - Sb_2Se_3 - Si$ meta-WP, Fig. 4 presents the DoLPs and the DoCPs of the transmitted beams for amorphous Sb_2Se_3 and the DoLPs and the AoLPs for crystalline Sb_2Se_3 under LCP and RCP excitations at the operation wavelength ranging from 1.5 to 1.6 μm. At the amorphous state, the transmitted beams exhibit high DoCPs approaching 1 and −1 under left and right CP (LCP and RCP) excitations, respectively, with relatively low DoLPs smaller than 0.195, within the wavelength range of 1.53 and 1.57 μm [Figs. 4(a) and 4(b)]. Specifically, the DoLPs are ~0.024 at the target wavelength of 1.55 μm, manifesting a well-distributed circular polarization [Fig. 4(g)]. Once Sb_2Se_3 transits into the crystalline state, the LCP and RCP incident beams are converted into −45 deg-oriented and 45 deg-oriented LP beams correspondingly [Figs. 4(d), 4(e) and 4(h)]. Meanwhile, the calculated DoLPs exceed 0.95 for both cases within the wavelength range of 1.53 and 1.57 μm. Moreover, the transmittance and conversion efficiency, defined as the intensity ratio between the transmitted light and incident light and the intensity ratio between the target polarized state light and incident light, exceed 93.7% and 92.8%, respectively, under CP excitations in the HWP mode, whereas in the QWP mode, they are above 90.6% and 88.1%, spanning the wavelengths from 1.53 to 1.57 μm [Figs. 4(c) and 4(f)]. Notably, at the target wavelength of 1.55 μm, both transmittance and conversion efficiency are nearly equal, reaching up to 95.7% and 94.8% in HWP and QWP modes, respectively.

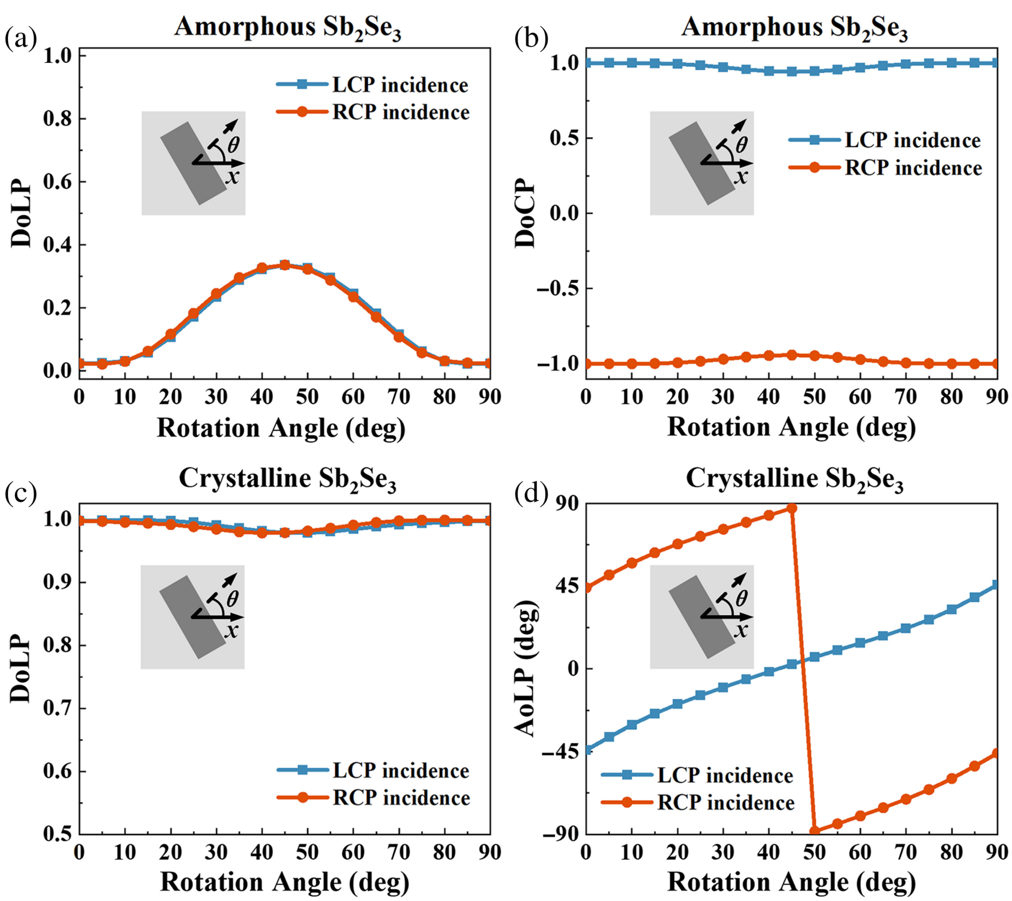

Fig. 5 Performance of the tunable meta-WP with different rotations relative to the x-axis. (a) DoLPs and (b) DoCPs of the transmitted beams under CP excitations at the amorphous state. (c) DoLPs and (d) AoLPs of the transmitted beams under CP excitations at the crystalline state.

Figure 5 shows the DoLPs and DoCPs of the transmitted beams for amorphous Sb_2Se_3 and the DoLPs and AoLPs of the transmitted beams for crystalline Sb_2Se_3 as a function of the rotation angle with respect to the x-axis at $\lambda = 1.55\ \mu m$. At the amorphous state, the incident CP beams are converted into their cross-polarized lights with high conversion ratios despite the rotation angle, indicated by the relatively low and high DoCPs (>0.925) [Figs. 5(a) and 5(b)]. When Sb_2Se_3 transits to the crystalline state, the DoLPs of transmitted beams stay above 0.975 without obvious changes, as shown in Fig. 5(c). As for the AoLPs, they change linearly with the rotation angle θ, demonstrating the orientation-independent property of the designed QWP. For instance, the AoLP is switched from −45 deg (45 deg) to 45 deg (−45 deg) when θ is rotated from 0 to 90 deg for the LCP (RCP) incidence. Therefore, the $Si-Sb_2Se_3-Si$ metasurface maintains consistent performance for different rotation angles, indicating its versatility for accomplishing more intricate functionalities.[1–3]

To dynamically manipulate the $Si-Sb_2Se_3-Si$ metasurface, we propose a practical electro-thermal phase control. As illustrated in Fig. 6(a), we analyze a meta-WP consisting of 10×10 $Si-Sb_2Se_3-Si$ meta-atoms. The Sb_2Se_3 bricks are uniformly heated by a 10 nm-thick graphene heater possessing excellent thermal and electrical conductivity.[33] Direct ohmic contact with the graphene layer is achieved via two 50 nm-thick gold electrodes. A coupled Multiphysics model, incorporating the electric currents module that simulates electric current distribution and heat transfer in the solid module that calculates the heating exchange and

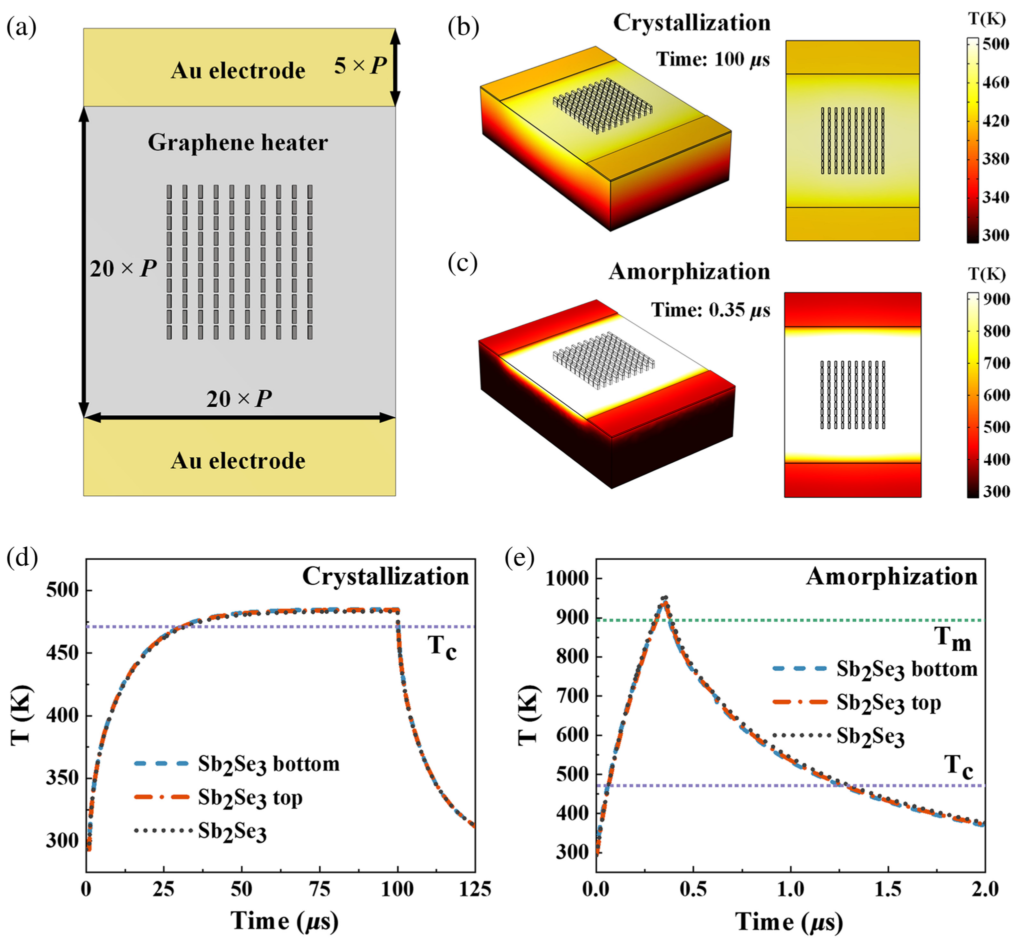

Fig. 6 Electro-thermal control of the $Si-Sb_2Se_3-Si$ meta-WP. (a) A schematic view of the tunable meta-WP driven by the electro-thermal control. (b) Simulated temperature profiles under a crystallization pulse with a bias voltage of 4.46 V and a pulse width of 100 μs. (c) Simulated temperature profiles model under an amorphization pulse with a bias voltage of 26.7 V and a pulse width of 350 ns. Temperature responses of the bottom surface, the top surface, and the entire volume of Sb_2Se_3 bricks during the (d) crystallization and (e) amorphization processes.

Table 1 Material properties used in electro-thermal simulation.

Material	Electrical conductivity ($S \cdot m^{-1}$)	Relative permittivity	Density ($kg \cdot m^{-3}$)	Hat capacity ($J \cdot kg^{-1} \cdot K^{-1}$)	Thermal conductivity ($W \cdot m^{-1} \cdot K^{-1}$)
$a\_Sb_2Se_3$	/	/	5810	$Cp(T)$[34]	0.36
$c\_Sb_2Se_3$	/	/	5810	$Cp(T)$[34]	0.57
Si	/	/	2329	700	130
SiO_2	/	/	2203	740	1.38
Graphene	$1/(d \times R_s)$[a]	4.708	2250	420	160
Au	45.6×10^6	6.9	19,300	129	317

[a]d is the thickness of graphene, R_s is the sheet resistance of 1936 Ω.

temperature distribution, was utilized. In the heat transfer module, infinite element domains are set as the side boundaries, and convective heat flux boundary conditions with an ambient temperature of $T = 293$ K are applied to the bottom surfaces of the model. Material properties essential for the electro-thermal simulation are detailed in Table 1.

With this model, the meta-WP undergoes phase transition with two distinct electrical pulses. Crystallization is initiated by heating Sb_2Se_3 above the crystalline temperature of $T_c = 473$ K using a long, low-voltage pulse of V_c. Specifically, a pulse voltage of 4.46 V and a width of 100 μs are employed in this simulation. Approximately 30 μs into the process, the entire Sb_2Se_3 array reaches full crystallization [Figs. 6(b) and 6(d)]. The temperature responses in Fig. 6(d) reveal a remarkably uniform distribution across the top surface, bottom surface, and the entire volume of Sb_2Se_3 bricks. On the other hand, amorphization requires a short- and high-voltage pulse of V_m to heat Sb_2Se_3 above the melting temperature of $T_m = 893$ K and then rapidly cool it down below the crystalline temperature T_c. In this case, a 26.7 V pulse with a 350 ns-long width is adopted. The entire array of Sb_2Se_3 meta-atoms undergoes rapid annealing above the melting temperature T_m, as illustrated in Figs. 6(c) and 6(e). Subsequently, it takes only ~900 ns for the array to rapidly cool down below the crystalline temperature T_c, which meets the requirement for effective amorphization of phase-change material.[35–37] As a result, the processing time for the re-amorphization of the entire array of Sb_2Se_3 meta-atoms is 1.25 μs, comprising 350 ns for annealing and 900 ns for cooling down. Moreover, by extracting the electric currents for crystallization and re-amorphization (i.e., 2.5 and 15 mA), the estimated energy required for the phase transition is ~1.115 and 0.1402 μJ, respectively, which provides a valuable reference for future experimental demonstrations.

3 Conclusion

In this work, we have utilized an array of periodic $Si-Sb_2Se_3-Si$ meta-atoms to realize a transmissive tunable metasurface exhibiting the switchable functionalities between an HWP and a QWP under two states of Sb_2Se_3 at the wavelength of 1.55 μm. The designed tunable meta-WP consistently excels across varied rotation angles, showcasing its versatility in enabling intricate functionalities within diverse designs. In addition, the feasibility of this tunable optical waveplate is convincingly verified through electro-thermal control, which exhibits effective and switchable phase changes of the Sb_2Se_3 meta-atom array with a graphene heater. The proposed tunable meta-WP could offer fascinating possibilities for developing low-loss and high-performance integrated adaptive photonic devices.

Code and Data Availability

All data in support of the findings of this paper are available within the article.

Acknowledgments

This work was funded by the National Natural Science Foundation of China (Grant Nos. 92373105 and 62074015), the 111 Project of China (Grant No. B14010), Villum Fonden (Grant No. 37372), and Danmarks Frie Forskningsfond (Grant No. 1134-00010B).

References

1. N. Yu and F. Capasso, "Flat optics with designer metasurfaces," *Nat. Mater.* **13**(2), 139–150 (2014).
2. F. Ding, A. Pors, and S. I. Bozhevolnyi, "Gradient metasurfaces: a review of fundamentals and applications," *Rep. Prog. Phys.* **81**(2), 026401 (2018).
3. F. Ding, Y. Yang, and S. I. Bozhevolnyi, "Dynamic metasurfaces using phase-change chalcogenides," *Adv. Opt. Mater.* **7**(14), 1801709 (2019).
4. J. T. Heiden et al., "Gap-surface plasmon metasurfaces for broadband circular-to-linear polarization conversion and vector vortex beam generation," *Adv. Opt. Mater.* **7**(9), 1801414 (2019).
5. Z. Tao et al., "Reconfigurable conversions of reflection, transmission, and polarization states using active metasurface," *Appl. Phys. Lett.* **110**(12), 121901 (2017).
6. Z. Wei et al., "Highly efficient beam steering with a transparent metasurface," *Opt. Express* **21**(9), 10739–10745 (2013).
7. Y. Deng et al., "Functional metasurface quarter-wave plates for simultaneous polarization conversion and beam steering," *ACS Nano* **15**(11), 18532–18540 (2021).
8. F. Ding, Y. Chen, and S. I. Bozhevolnyi, "Focused vortex-beam generation using gap-surface plasmon metasurfaces," *Nanophotonics* **9**(2), 371–378 (2020).
9. F. Yue et al., "Vector vortex beam generation with a single plasmonic metasurface," *ACS Photonics* **3**(9), 1558–1563 (2016).
10. T.-J. Cui, S. Liu, and L.-L. Li, "Information entropy of coding metasurface," *Light: Sci. Appl.* **5**(11), e16172 (2016).
11. L. Huang, S. Zhang, and T. Zentgraf, "Metasurface holography: from fundamentals to applications," *Nanophotonics.* **7**(6), 1169–1190 (2018).
12. A. Li, S. Singh, and D. Sievenpiper, "Metasurfaces and their applications," *Nanophotonics.* **7**(6), 989–1011 (2018).
13. M. I. Shalaev et al., "High-efficiency all-dielectric metasurfaces for ultracompact beam manipulation in transmission mode," *Nano Lett.* **15**(9), 6261–6266 (2015).
14. L. Yang et al., "High-efficiency all-dielectric transmission metasurface for linearly polarized light in the visible region," *Photonics Res.* **6**(6), 517–524 (2018).
15. W. Yang et al., "All-dielectric metasurface for high-performance structural color," *Nat. Commun.* **11**(1), 1864 (2020).
16. I. Staude et al., "Tailoring directional scattering through magnetic and electric resonances in subwavelength silicon nanodisks," *ACS Nano* **7**(9), 7824–7832 (2013).
17. C. Ruiz de Galarreta et al., "Reconfigurable multilevel control of hybrid all-dielectric phase-change metasurfaces," *Optica* **7**(5), 476–484 (2020).
18. F. Ding, Y. Chen, and S. I. Bozhevolnyi, "Gap-surface plasmon metasurfaces for linear-polarization conversion, focusing, and beam splitting," *Photonics Res.* **8**(5), 707–714 (2020).
19. J. Sautter et al., "Active tuning of all-dielectric metasurfaces," *ACS Nano* **9**(4), 4308–4315 (2015).
20. A. Komar et al., "Electrically tunable all-dielectric optical metasurfaces based on liquid crystals," *Appl. Phys. Lett.* **110**(7), 071109 (2017).
21. A. Komar et al., "Dynamic beam switching by liquid crystal tunable dielectric metasurfaces," *ACS Photonics* **5**(5), 1742–1748 (2018).
22. M. Rahmani et al., "Reversible thermal tuning of all-dielectric metasurfaces," *Adv. Funct. Mater.* **27**(31), 1700580 (2017).
23. T. Lewi, N. A. Butakov, and J. A. Schuller, "Thermal tuning capabilities of semiconductor metasurface resonators," *Nanophotonics* **8**(2), 331–338 (2018).
24. Z. Cai et al., "Phase-change metasurface for switchable waveplates," in *AOPC 2022: Optoelectron. and Nanophotonics* (2023).
25. D.-Q. Zhang et al., "Tunable wave plates based on phase-change metasurfaces," *Opt. Express* **29**(5), 7494–7503 (2021).
26. D.-Q. Zhang et al., "Tunable dielectric metasurfaces by structuring the phase-change material," *Opt. Express* **30**(3), 4312–4326 (2022).
27. C. H. Chu et al., "Active dielectric metasurface based on phase-change medium," *Laser Photonics Rev.* **10**(6), 986–994 (2016).
28. M. Delaney et al., "A new family of ultralow loss reversible phase-change materials for photonic integrated circuits: Sb_2S_3 and Sb_2Se_3," *Adv. Funct. Mater.* **30**(36), 2002447 (2020).

29. Z. Cai et al., "Dynamic dual-functional optical wave plate based on phase-change meta-molecules," *Opt. Lett.* **48**(14), 3685–3688 (2023).
30. Z. Cai et al., "Dynamic phase-change metawaveplates for advanced wavefront shaping," *Adv. Photonics Res.* **3**(12), 2200261 (2022).
31. Z. Fang et al., "Non-volatile reconfigurable silicon photonics based on phase-change materials," *IEEE J. Sel. Top. Quantum Electron.* **28**(3), 1–17 (2021).
32. S.-M. F. Nee, "Polarization measurement," in *Measurement, Instrumentation, and Sensors Handbook*, pp. 49-41–49-24, CRC Press, Boca Raton, Florida (2017).
33. O. Abed and L. Yousefi, "Tunable metasurfaces using phase change materials and transparent graphene heaters," *Opt. Express* **28**(23), 33876–33889 (2020).
34. O. Madelung, "Non-tetrahedrally bonded elements and binary compounds I," in *Landolt-Börnstein-Group III Condensed Matter*, Springer-Verlag, Heidelberg, Germany (1998).
35. O. Hemmatyar et al., "Enhanced meta-displays using advanced phase-change materials," arXiv:12159 (2021).
36. C. Ríos et al., "Ultra-compact nonvolatile phase shifter based on electrically reprogrammable transparent phase change materials," *PhotoniX* **3**(1), 26 (2022).
37. S. Zhuo et al., "Dynamic transmissive metasurface for broadband phase-only modulation based on phase-change materials," *Laser Photonics Rev.* **17**(1), 2200403 (2023).

Xingling Pan received her BS degree from Beijing Institute of Technology, China, in 2022. Currently, she is pursuing her doctorate in the field of optical metasurfaces at the School of Integrated Circuits and Electronics, Beijing Institute of Technology, China.

Zhiming Chen received his BEng degree in electronic science and technology from Tsinghua University, Beijing, China, in 2007 and his PhD in electrical and computer engineering from the University of California at Irvine, Irvine, California, United States, in 2012. In spring 2012, he joined the Beijing Institute of Technology, Beijing, as a faculty member, where he is currently a professor with the School of Integrated Circuits and Electronics. His research interests include millimeter-wave (MMW) integrated circuit design, advanced packaging, and metasurface.

Yingtao Ding received her PhD in mechanics from Tsinghua University, China. She was a post-doctoral research fellow at the Institute of Microelectronics, Tsinghua University, from 2003 to 2005. In 2005, she joined the Beijing Institute of Technology, where she is currently a professor at the School of Integrated Circuits and Electronics. Her research interests include optical meta-surface, MEMS sensors, actuators, and 3D integration.

Fei Ding received his PhD in optical engineering from Zhejiang University, China, in 2015. Currently, he is an associate professor at the University of Southern Denmark. His current research interests include metasurfaces, plasmonics, and quantum nanophotonics. He has published more than 75 articles in peer-reviewed journals. He won the Wang Daheng Optical prize, the Young Scientist Award from the Progress in Electromagnetics Research Symposium, Villum Young Investigator, and the DOPS award.

Biographies of the other authors are not available.